Received: 18 January 2022 | Revised: 9 March 2022 | Accepted: 13 March 2022

DOI: 10.1002/cey2.207

RESEARCH ARTICLE

CARBON ENERGY WILEY

A sulfur self-doped multifunctional biochar catalyst for overall water splitting and a supercapacitor from Camellia japonica flowers

Chengkai Xia[1] | **Subramani Surendran**[2,3] | **Seulgi Ji**[4] | **Dohun Kim**[3] | **Yujin Chae**[3] | **Jaekyum Kim**[1] | **Minyeong Je**[4] | **Mi-Kyung Han**[3,5] | **Woo-Seok Choe**[1] | **Chang Hyuck Choi**[6] | **Heechae Choi**[4] | **Jung Kyu Kim**[1] | **Uk Sim**[2,3,5]

[1]School of Chemistry Engineering, Sungkyunkwan University, Suwon, Republic of Korea

[2]Hydrogen Energy Technology Laboratory, Korea Institute of Energy Technology (KENTECH), Naju, Republic of Korea

[3]Department of Materials Science & Engineering, Chonnam National University, Gwangju, Republic of Korea

[4]Theoretical Materials & Chemistry Group, University of Cologne, Cologne, Germany

[5]Research Institute, NEEL Sciences, Inc., Naju, South Korea

[6]Department of Chemistry, Pohang University of Science and Technology (POSTECH), Gyeongsangbuk-do, Republic of Korea

Correspondence

Uk Sim, Hydrogen Energy Technology Laboratory, 200 Hyeoksin-ro, Naju, Jeonnam 58330, Republic of Korea.
Email: usim@kentech.ac.kr

Jung Kyu Kim, School of Chemical Engineering Sungkyunkwan University, 2066 Seobu-ro, Jangan-gu, Suwon 16419, Republic of Korea.
Email: legkim@skku.edu

Heechae Choi, Theoretical Materials & Chemistry Group, Institute of Inorganic Chemistry,University of Cologne, Greinstr. 6, 50939 Cologne, Germany.
Email: h.choi@uni-koeln.de

Chang Hyuck Choi, Department of Chemistry Pohang University of Science and Technology (POSTECH)77, Cheongam-ro, Nam-gu, Pohang-si, Gyeongsangbuk-do, Republic of Korea.
Email: chchoi@postech.ac.kr

Abstract

A versatile use of a sulfur self-doped biochar derived from Camellia japonica (camellia) flowers is demonstrated as a multifunctional catalyst for overall water splitting and a supercapacitor. The native sulfur content in the camellia flower facilitates in situ self-doping of sulfur, which highly activates the camellia-driven biochar (SA-Came) as a multifunctional catalyst with the enhanced electron-transfer ability and long-term durability. For water splitting, an SA-Came-based electrode is highly stable and shows reaction activities in both hydrogen and oxygen evolution reactions, with overpotentials of 154 and 362 mV at 10 mA cm^{-2}, respectively. For supercapacitors, SA-Came achieves a specific capacitance of 125.42 F g^{-1} at 2 A g^{-1} and high cyclic stability in a three-electrode system in a 1 M KOH electrolyte. It demonstrated a high energy density of 34.54 Wh kg^{-1} at a power density of 1600 W kg^{-1} as a symmetric hybrid supercapacitor device with a wide working potential range of 0–1.6 V.

KEYWORDS

activated carbon, biomass, supercapacitor, sustainable chemistry, water splitting

Chengkai Xia, Subramani Surendran, and Seulgi Ji contributed equally to this study.

This is an open access article under the terms of the Creative Commons Attribution License, which permits use, distribution and reproduction in any medium, provided the original work is properly cited.

© 2022 The Authors. *Carbon Energy* published by Wenzhou University and John Wiley & Sons Australia, Ltd.

Funding information
National Research Foundation of Korea, Grant/Award Numbers: 2016M3D1A1021141, 2020R1A2C2006077, 2022R1A2C1012419, 2021R1A4A1024129, 2021R1A5A1030054; Ministry of Trade, Industry and Energy (MOTIE, Korea), Grant/Award Number: 20213030040590

1 | INTRODUCTION

With the growing public concern about environmental protection and climate change, advanced conversion and storage technologies for green energy have become a research hotspot worldwide.[1–4] In the field of energy conversion, because hydrogen (H_2) fuel with high energy density can be directly produced from water, electrocatalytic water-splitting based on the hydrogen evolution reaction (HER) and the oxygen evolution reaction (OER) is considered a new promising technology.[5–7] Energy storage devices, in particular supercapacitors, with a rapid charge/discharge rate and a long cycling life, have received considerable attention. To date, noble metal-based catalysts (Pt, Ir, and Ru) are still the most widely used water-splitting catalysts.[8–10] Because commercial hydrogen production requires cheap and earth-abundant electrocatalysts, the high cost of noble metal-based catalysts limits their development in this field.[11] Likewise, supercapacitors are also facing this problem, as the existing energy storage materials are still dominated by noble metal-based catalysts.[12–15] Therefore, novel low-cost and high-performance electrode materials need to be developed for the commercial application of electrochemical water splitting for H_2 production and supercapacitors.[16–18]

Carbon-based materials have been proven to be a reasonable alternative to noble metal-based materials for energy applications. Carbon materials, including activated carbon,[19] graphene,[20] carbon nanotubes,[21] and carbide-derived carbons,[22] have been widely studied as electrode materials for supercapacitors and electrochemical water splitting. Thus, the development of multifunctional carbon-based materials to simultaneously achieve water splitting and energy storage applications has also become a feasible target.[23] However, most of the existing carbon materials are still highly dependent on mineral raw materials and petroleum products in their synthesis and cannot perfectly fulfill the requirements of green chemistry.[24–26] Considering the major environmental problems faced by humanity at present, biochar, as a regenerable activated carbon produced from biomass via modern pyrolysis processes, is worth exploring.[27] In addition to the inherent advantages of low cost and environmental friendliness,[28] biochar usually has a self-doping effect during the pyrolysis process, which can lead to spontaneous doping of nitrogen, sulfur, and phosphorus heteroatoms on their carbon skeleton, which results in promising electrochemical activity.[29] In general, by introducing exogenous heteroatoms into a highly ordered carbon skeleton, the electrochemical capacity of the original π–electron network can be adjusted, resulting in an unbalanced electroactive state to provide greater electrocatalytic activity.[30] Compared with the complex heteroatom doping strategies that need to be adopted in artificial carbon materials for modification, biochar is attractive because a heteroatom-doped carbon skeleton can be obtained based on a simple synthesis strategy through the self-doping effect. Numerous biomass sources, such as bean sprouts,[31] poplar catkin,[32] watermelon rind,[33] and coffee waste,[34] have been investigated for the synthesis of self-doped biochar. Camellia japonica (camellia) is an ornamental flower that is widely distributed in East Asia. Considering that the camellia is rich in anionic heteroatoms, it can be a valuable biomass feedstock for the synthesis of biochar.[35,36]

In this study, sulfur self-doped activated camellia (SA-Came) nanospheres were prepared using a solvothermal–pyrolysis method with camellia flowers as raw materials. During the process, sulfur atoms were naturally doped into the carbon nanospheres without additional doping precursors. The SA-Came nanospheres showed remarkable electrocatalytic activity in both HER and OER with overpotentials of 154 and 362 mV, respectively, to reach a current density of 10 mA cm^{-2}. When applied for overall water splitting on a dual-electrode system, an output voltage of only 1.76 V was needed to reach 10 mA cm^{-2}. Moreover, the as-prepared SA-Came nanosphere electrode showed a specific capacitance of 125.42 F g^{-1} at 2 A g^{-1} and high cyclic stability in a three-electrode system in a 1 M KOH electrolyte. This study demonstrates that sulfur self-doped biochar derived from waste camellia flowers can be applied as a multifunctional electrocatalyst for energy conversion/storage with outstanding electrochemical performance.

2 | EXPERIMENTAL SECTION

2.1 | Synthesis of S-ACame nanospheres

Naturally falling camellia flowers were collected from local camellia bushes at Chonnam University (Gwangju, South Korea). Subsequently, the separated petals were sun-dried for 2 days and ground. The as-prepared powder (3 g) was dispersed in 60 mL of 1 M H_2SO_4 (ACS reagent, 95.0%–98.0%; Sigma-Aldrich) in a Teflon-lined autoclave and placed in a muffle furnace at 180°C for 24 h. The obtained sulfur-doped camellia powder was centrifuged and thoroughly washed with deionized water and ethanol, and then dried in a vacuum at 80°C overnight; the obtained sample was labeled S-Came. The S-Came was activated by mixing it with KOH (ACS reagent, ≥85%; Sigma-Aldrich) at a volume ratio of 1:1 in deionized water under constant stirring for 24 h, followed by washing and drying at 80°C for 12 h. The KOH-activated sample was carbonized in a horizontal tube furnace at 800°C for 2 h under an N_2 atmosphere at a heating rate of 5°C min^{-1}; this final product was labeled SA-Came. Additionally, the experimental conditions were optimized by carbonizing the samples at various temperatures (800°C and 900°C) under different Ar atmospheres. The resultant samples were named SA-Came(A8) and SA-Came(A9), respectively. Here, the alphabet represents the Ar atmospheric conditions, while the number denotes the applied temperature (800C & 900°C).

2.2 | Characterizations

The morphology and elemental map features were estimated by field emission scanning electron microscopy (FE-SEM, S-4700; Hitachi) and transmission electron microscopy (TEM; Tecnai F20 ST; FEI) using an energy-dispersive X-ray spectroscopy (EDS) module. The phase formation and structure were studied using powder X-ray diffraction (XRD) (Rint 1000; Rigaku) and laser Raman spectrophotometry (NRS-5100; Jasco). The chemical bonding between the elements was observed and measured by X-ray photoelectron spectroscopy (XPS; Multilab 2000). A multichannel potentiostat (VMP3-Biologic) was used to determine the electrochemical properties.

2.3 | Electrochemical measurements

The electrocatalytic properties of the samples were determined at a temperature of 25°C using a 1 M KOH aqueous electrolyte in two- and three-electrode systems. The working electrodes were prepared by mixing the as-prepared samples, polyvinylidene difluoride, and carbon black at a mass ratio of 8:1:1 in *N*-methyl-2-pyrrolidone and loading them onto nickel foam substrates. Thereafter, the electrodes were oven-dried overnight at 80°C. In the three-electrode system, a Hg/HgO electrode and a graphite rod were used as the reference electrode and the counter electrode, respectively. The potential of the electrocatalytic reaction was converted into a reversible hydrogen electrode (RHE) according to the following equation:

$$E_{RHE} = E_{(Hg/HgO)} + 0.118 + 0.059\,pH.$$

3 | RESULTS AND DISCUSSION

3.1 | Carbonization

At high temperatures, various organic substances present in camellia flowers undergo a series of physical and chemical transformations. Therefore, to determine the carbonization temperature, thermogravimetric differential thermal analysis (TG-DTA) was conducted on camellia flowers activated by KOH. As shown in Figure S1, the activated camellia showed an initial weight loss of approximately 5.5%—from 30°C to 100°C. This weight loss is mainly attributed to the evaporation of water from the sample. In the temperature range of 100–400°C, with the thermal decomposition of the remaining cellulose and hemicellulose after the KOH hydrothermal treatment,[37,38] a slight weight reduction of approximately 3.5% was observed. When the temperature was higher than 400°C, the TG curve showed a linear decrease in mass with the temperature, which indicated that the carbon skeleton started to decompose.[39,40] The trend of mass decrease shown in the TG curve is consistent with the exothermic behavior of activated camellia shown in the DTA curve. According to the TG–DTA characterization curves, 800°C was selected as the carbonization temperature to optimize the carbonization of the activated camellia. Because the determination of the optimal carbonization temperature is not the aim of this study, we did not compare the effects of different carbonization temperatures on the electrochemical performance of the final product.

3.2 | Characterization of activated carbon

SA-Came was successfully prepared using a simple chemical activation process using camellia flowers, as shown in Figure 1A. Furthermore, the electrochemical performance of the synthesized S-Came and SA-Came as a supercapacitor

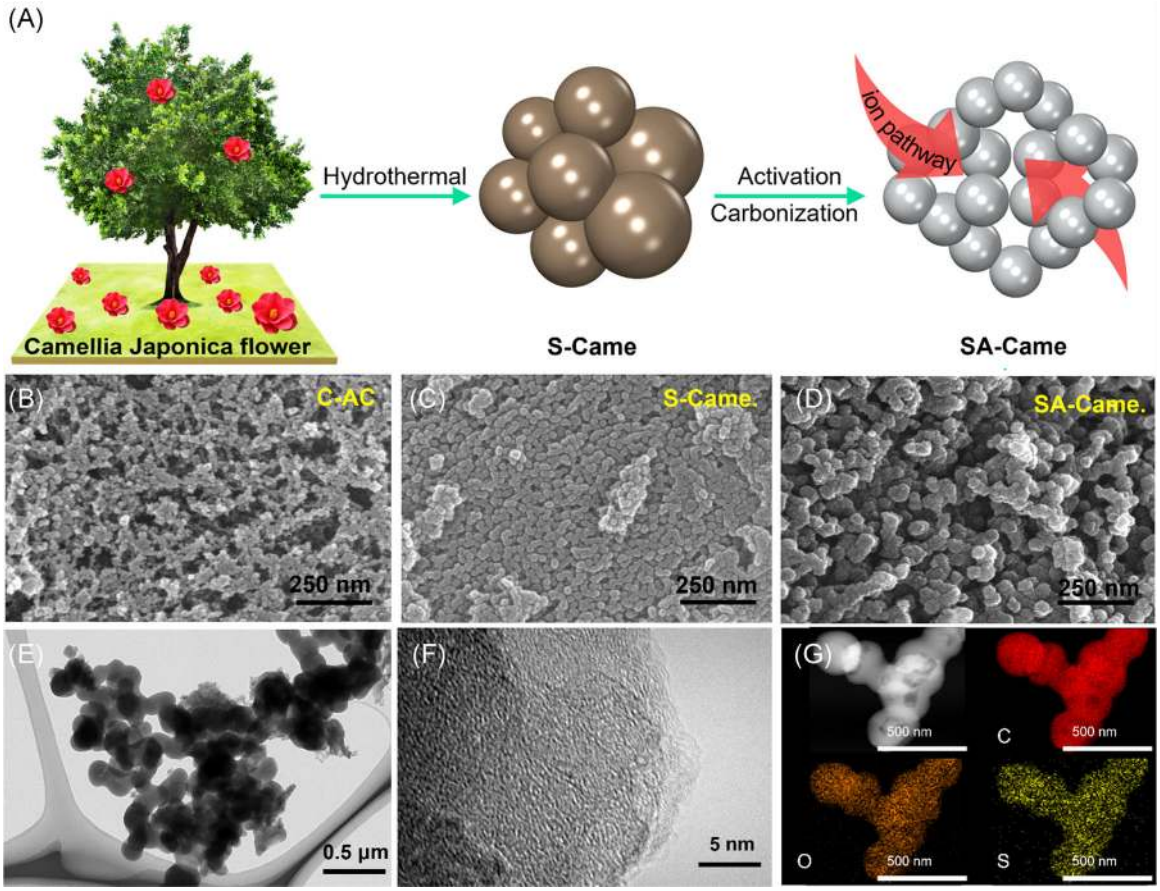


FIGURE 1 (A) Schematic for the preparation of the S-Came and SA-Came nanospheres. FE-SEM images of (B) C-AC, (C) S-Came, and (D) SA-Came. (E,F) Transmission electron microscopy images of SA-Came at various magnifications and (G) energy-dispersive X-ray spectroscopy mapping images of the SA-Came nanospheres. C-AC, commercially available activated carbon; FE-SEM, field emission scanning electron microscopy; S-Came, sulfur-doped camellia; SA-Came, sulfur self-doped activated camellia

electrode was studied and compared with that of commercially available activated carbon (C-AC; Yakuri).

The surface morphologies of all samples were confirmed using FE-SEM and TEM. Figure 1B–D shows FE-SEM images of C-AC, S-Came, and SA-Came powders. The SEM images of the three samples showed similar interconnected spherical morphologies. The formation mechanism of uniform carbon spheres of camellia flower via hydrothermal treatment involves three major processes: (i) dehydration, (ii) polymerization, and (iii) carbonization.[41–43] During the dehydration process, organic compounds such as cellulose, monosaccharides, acids, and phenolic compounds in the ground camellia powder decompose and dehydrate into reactive monomers like furan compounds.[43,44] The presence and composition of the organic compounds in the camellia flower play a crucial role in generating uniform carbon spheres via hydrothermal treatment.[45,46] The monomers react to form functionalized aromatic molecules via condensation and polymerization processes.[41,42] Finally, the powders were subjected to high-temperature carbonization treatment to produce the desired uniform carbon spheres. Thus, the hydrothermal treatment of camellia flowers revealed distinct uniform spherical shapes and size distributions. The microsphere structure of C-AC had an average diameter of approximately 18 nm and that of S-Came was approximately 26 nm. After carbonization, the particle size significantly increased because the carbon nanospheres agglomerated at high temperatures; in SA-Came, the particle size was approximately 50 nm. The morphology of the SA-Came nanospheres was a spherical structure with a rough surface and nanopores. The formation of a large number of nanopores leads to an increase in the number of micropores and mesopores, which increases the surface area and pore volume and is essential for charge transfer in electrochemical reactions. The formation of nanospheres in SA-Came was confirmed by TEM results, showing an amorphous carbon structure (Figure 1E,F). Moreover, as shown in Figure 1G, EDS mapping of SA-Came indicated that S was uniformly distributed on the surface of the samples. In addition, to ensure the stable

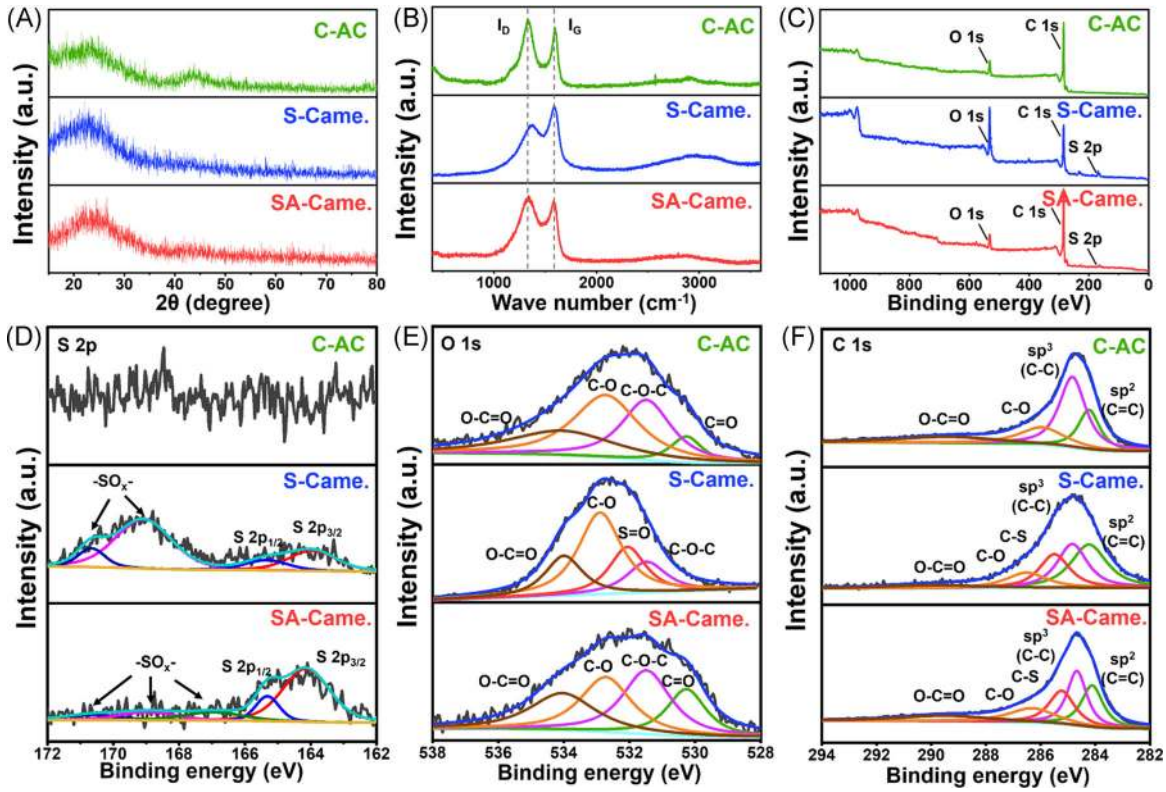


FIGURE 2 (A) X-ray diffraction patterns and (B) Raman spectra of the C-AC, S-Came, and SA-Came samples. (C) Full-range XPS spectra, (D) S 2p, (E) O 1s, and (F) C 1s XPS spectra of the C-AC, S-Came, and SA-Came samples. C-AC, commercially available activated carbon; S-Came, sulfur-doped camellia; SA-Came, sulfur self-doped activated camellia; XPS, X-ray photoelectron spectroscopy

content of sulfur atoms doped in each batch of samples, we have determined the elemental composition for two batches of samples prepared at separate intervals through energy-dispersive X-ray spectroscopy analysis (Figure S2). The sulfur contents in the SA-Came batch 1 and batch 2 samples were identified to be 5.32 and 5.76 wt%, respectively. This result confirms the reproducibility of the self-doped sulfur in SA-Came.

XRD analysis was performed to confirm the crystallographic structures of C-AC, S-Came, and SA-Came; the results are shown in Figure 2A. Only two broad peaks were observed in all three of these samples at 23.1° and 43.6°, which, respectively, belong to the (0 0 2) and (1 0 1) planes in the disordered graphitic structure.[47] Raman spectra were further explored to verify the chemical structure and degree of disorder, as shown in Figure 2B. All the spectra (C-AC, S-Came, and SA-Came) showed two distinct peaks: the D band at approximately 1330 cm^{-1} and the G band at approximately 1580 cm^{-1}, which signified disordered carbon and graphitic carbon, respectively. Generally, the integrated intensity ratio at the D and G bands (I_D/I_G) is used to represent the degree of structural disorder of a material.[48,49]

The I_D/I_G values of C-AC, S-Came, and SA-Came were 1.03, 0.88, and 1.01, respectively. Compared to that of S-Came, the higher I_D/I_G value of SA-Came demonstrated that the proportion of disordered carbon in the structure of the sample increased when the sample was subjected to persistent activation and pyrolysis. The formation of these disordered carbon structures is beneficial for generating more activation sites and promoting electrical conductivity, thereby improving electrochemical performance.[50]

XPS was performed to analyze the surface states and elemental compositions of the activated camellia flower and the carbon samples. As shown in the full-scan spectra (Figures S3 and 2C), raw camellia contained various elements, such as Na, Ca, P, and N, in addition to C, O, and S. After activation and carbonization, most of the trace elements were removed with the decomposition of organics, and only C, O, and S elements could be detected. To confirm that the hydrolysis treatment by H_2SO_4 would not introduce additional S atoms into the SA-Came sample, as a reference, KOH was used to activate the camellia flower directly, and the obtained sample was characterized via XPS. As shown in Figure S4, corresponding peaks appeared in the S 2p spectrum of this sample at the same binding energy, proving that the doped S atoms in SA-Came come from camellia flowers. The S 2p XPS spectra of the C-AC, S-Came, and SA-Came samples are shown in Figure 2D. The S 2p spectra of C-AC did not have any broad peaks, which

confirmed that the C-AC sample did not contain sulfur. The high-resolution S 2p XPS spectra of S-Came and SA-Came were deconvoluted into four peaks. The peaks located at 164.0 and 165.3 eV are, respectively, related to C–S bonding and attributed to S $2p_{3/2}$ and S $2p_{1/2}$. The other peaks located at 166.9, 168.9, and 170.1 eV correspond to various -SO_x^- species, such as $R_2S{=}O$, SO_3^{2-}, SO_4^{2-}, and RSO_3H.[51,52] The spectrum of S-Came showed higher intensity at the peaks attributable to -SO_x^- species, whereas the peak attributable to C–S bonding in the spectrum of SA-Came showed higher intensity. This indicates that the S element in the S-Came sample mainly exists in the sulfur–oxygen groups, whereas S atoms in the SA-Came sample are directly incorporated through the C–S bonding into the carbon framework. The incorporation of S atoms into the carbon framework promotes charge transfer between the electrolyte and the electrode, thus enhancing the energy capacitive properties.[53] Moreover, naturally substituted S sites provide more polarized surfaces with high activation sites, which are expected to improve the electrochemical performance.[54–56]

In Figure 2E, all the deconvoluted O 1s spectra of these three samples showed four peaks at 530.2 eV (C=O), 531.4 eV (C–O–C), 532.7 eV (C–O), and 534.0 eV (O–C=O), whereas the S-Came and SA-Came samples showed another peak corresponding to S=O bonding at 532.0 eV. The intensity of the deconvoluted peak of the S=O bonding in the S-Came spectrum was higher than that in the SA-Came spectrum, which also verifies the different bonding modes of S in these two samples. For the deconvolution of C 1s spectra (Figure 2F), four peaks at binding energies of 284.1, 284.7, 286.0, and 289.9 eV should correspond to the standard sp^2-hybridized C=C, sp^3 hybridized C–C, C–O, and O–C=O components, respectively.[57–59] S-Came and SA-Came had a deconvoluted peak at 285.2 eV, corresponding to C–S bonding. The C–S peak in the SA-Came spectra had a higher intensity, which is consistent with the deconvolution result for the S 2p spectrum.

The electrochemical property of the prepared SA-Came: Electrochemical impedance spectroscopy (EIS) analysis was performed to investigate the ion diffusion kinetics at the electrode–electrolyte interface. The EIS of SA-Came, S-Came, and C-AC was conducted from 100 kHz to 0.01 Hz at the open circuit potential, and the Nyquist plot is shown in Figure 3A. The Nyquist plot revealed a semicircle curve, including electrolyte resistance (R_s) and charge-transfer

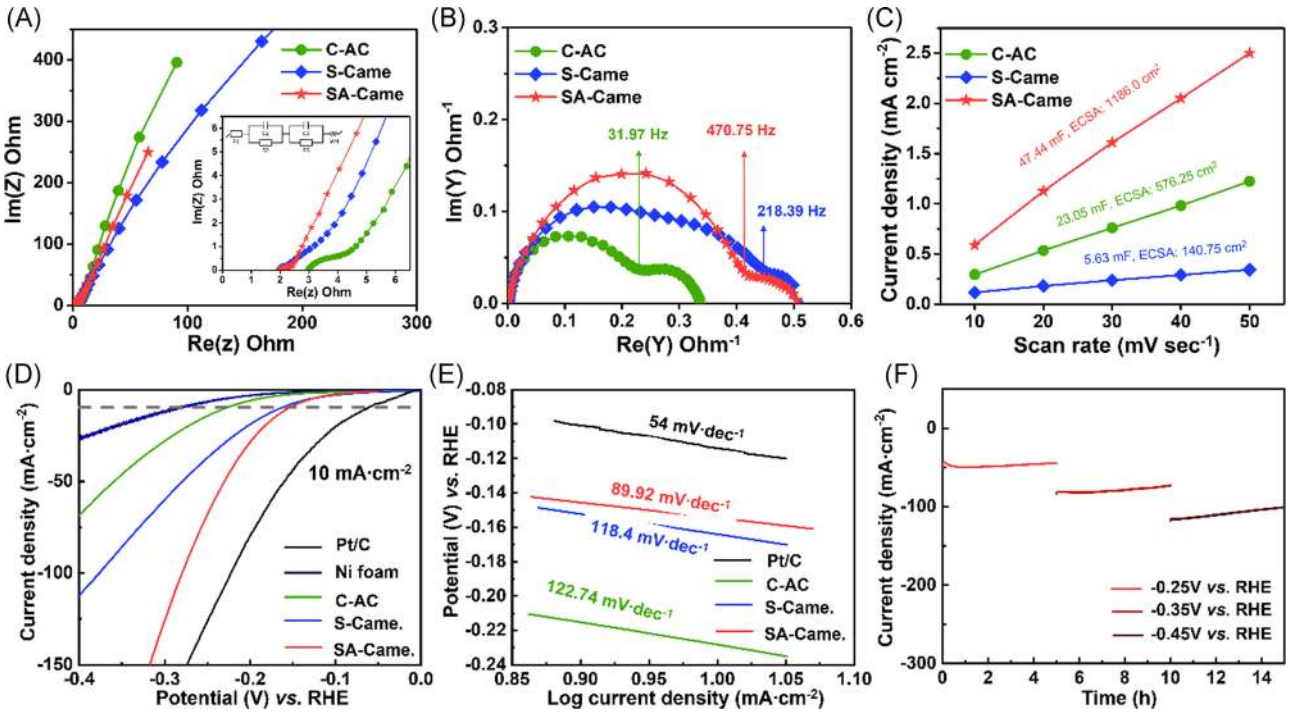


FIGURE 3 (A) Nyquist impedance plot of C-AC, S-Came, and SA-Came. The inset shows the EIS at high frequency. (B) Nyquist admittance plot of C-AC, S-Came, and SA-Came, (C) the capacitance current of C-AC, S-Came, and SA-Came at scan rates of 10–50 mV s^{-1}, (D) HER LSV curves, (E) HER Tafel slopes of the bare Ni foam, C-AC, S-Came, and SA-Came, and (F) CA curves of SA-Came at various applied potentials for HER. C-AC, commercially available activated carbon; CA, chronoamperometry; EIS, electrochemical impedance spectroscopy; HER, hydrogen evolution reaction; LSV, linear sweep voltammetry; S-Came, sulfur-doped camellia; SA-Came, sulfur self-doped activated camellia

resistance (R_{ct}) in the high-frequency range, while a vertical line of the Nyquist plot indicated the ion diffusion within the electrode in the low-frequency range. The estimated R_s and R_{ct} values of SA-Came were 1.90 and 0.27 Ω, which were less than those of C-AC (3.0 and 0.77 Ω) and S-Came (2.06 and 0.33 Ω), respectively (inset in Figure 3A). The lower R_s and R_{ct} values induce faster ion diffusion rates, and the shorter vertical line at SA-Came those at C-AC and S-Came confirms the faster ion-transfer behavior between the electrolyte and the electrode. The admittance plots from the EIS curve of SA-Came, S-Came, and C-AC are shown in Figure 3B. The knee frequency induced by the admittance plot is demonstrated as the maximum frequency wherein resistance can be negligible, and the capacitive reaction is dominant. Thus, the knee frequency of SA-Came (470.75 Hz) is higher than those of C-AC (31.97 Hz) and S-Came (218.39 Hz), showing that the former has a lower charge-transfer resistance than the latter two. Furthermore, to comprehensively understand the electrocatalytic activity, the electrochemical specific surface area (ECSA) was measured to demonstrate the activity of the electrocatalysts. As shown in Figure 3C, the C_{dl} values of C-AC, S-Came, and SA-Came were 5.63, 23.05, and 47.44 mF cm^{-2}, respectively. Theoretically, the larger the ECSA, the more the active sites present in the electrocatalyst in the corresponding reaction, which leads to more effective electron transfer. Therefore, this further explains why the SA-Came electrocatalyst showed the best HER performance among the as-synthesized materials: the SA-Came electrocatalyst had a larger electrochemical surface area and more reaction active sites, thereby yielding higher reaction kinetics.

The electrochemical performance was evaluated to determine the hydrogen production performance and energy storage capability of the prepared SA-Came, S-Came, and C-AC electrodes in a conventional three-electrode configuration using a 1 M KOH aqueous electrolyte. The electrocatalytic HER activities of the C-AC, S-Came, and SA-Came electrocatalysts were tested via linear sweep voltammetry (LSV). A commercial Pt/C catalyst was also used as an electrochemical hydrogen production anode material for reference. As shown in Figure 3D, as the best known HER catalyst, Pt/C has the lowest HER overpotential of 63 mV at 10 mA cm^{-2}. Interestingly, SA-Came showed superior HER performance, reaching a current density of approximately 300 mA cm^{-2} at a nominal applied potential, and the SA-Came anode showed the highest HER activity with the lowest overpotential, except for commercial Pt/C, for achieving a current density of 10 mA cm^{-2}.

The overpotentials of the nickel foam, C-AC, S-Came, and SA-Came anodes were 282.7, 228, 166, and 154 mV, respectively, at 10 mA cm^{-2}. In addition, the HER LSV curves of SA-Came prepared under different experimental conditions were also constructed, as shown in Figure S5. SA-Came(A9) (174.6 mV) and SA-Came(A8) (187.6 mV) showed much higher overpotentials than SA-Came (154 mV) at a current density of 10 mA cm^{-2}, respectively. Moreover, as shown in Figure 3E, the SA-Came anode showed the smallest Tafel slope of 89.92 mV dec^{-1} among the as-synthesized carbon-based electrocatalysts, which indicates the superior HER catalytic kinetics. The chronoamperometry of SA-Came was measured at various potential ranges from −0.25 to −0.45 V (vs. RHE) with a step of −0.1 V (vs. RHE), which was retained over 50,000 s (Figure 3F). The negligible changes observed for the chronoamperometry curves of SA-Came highlight its durability against HER in highly alkaline aqueous electrolytes. As shown in Figure S6, the XPS results after HER show that the surface state of the SA-Came electrocatalyst during the HER process changed, which can be considered the result of surface activation. The most significant change was that the intensity of the C–C and C–S peaks decreased after the reaction, and the intensity of the C–O and S═O peaks increased significantly. This phenomenon was attributed to the combination of the –OH groups with the C–C and C–S bonds during the reaction. This also shows that the carbon skeleton was doped with sulfur to produce C–S bonds, which promoted the adsorption of –OH groups on the surface of the electrocatalyst during the HER process and provided more reactive sites. This was further confirmed by electrochemical characterization.

Additionally, when it was used as an anode material, SA-Came also showed reaction activity in OER. As shown in Figure S7, SA-Came showed a low overpotential (340 mV) for a current density of 10 mA cm^{-2}, and its Tafel slope was 86.01 mV dec^{-1}. With the remarkable reaction activity in both HER and OER, a lab-scale overall water-splitting system was fabricated (as shown in Figure 4A) using SA-Came as both the anode and the cathode in a 1 M KOH aqueous solution. The LSV curve indicated an overpotential value of 530 mV at a current density of 10 mA cm^{-2} (Figure 4B), and the fabricated SA-Came electrodes showed considerable stability for 24 h (Figure 4C). Compared to other artificial sulfur-doped carbon catalysts (Figure 4D), SA-Came had a comparable overpotential and the lowest total value, thereby demonstrating that SA-Came is an excellent bifunctional catalyst for water splitting.[60–65]

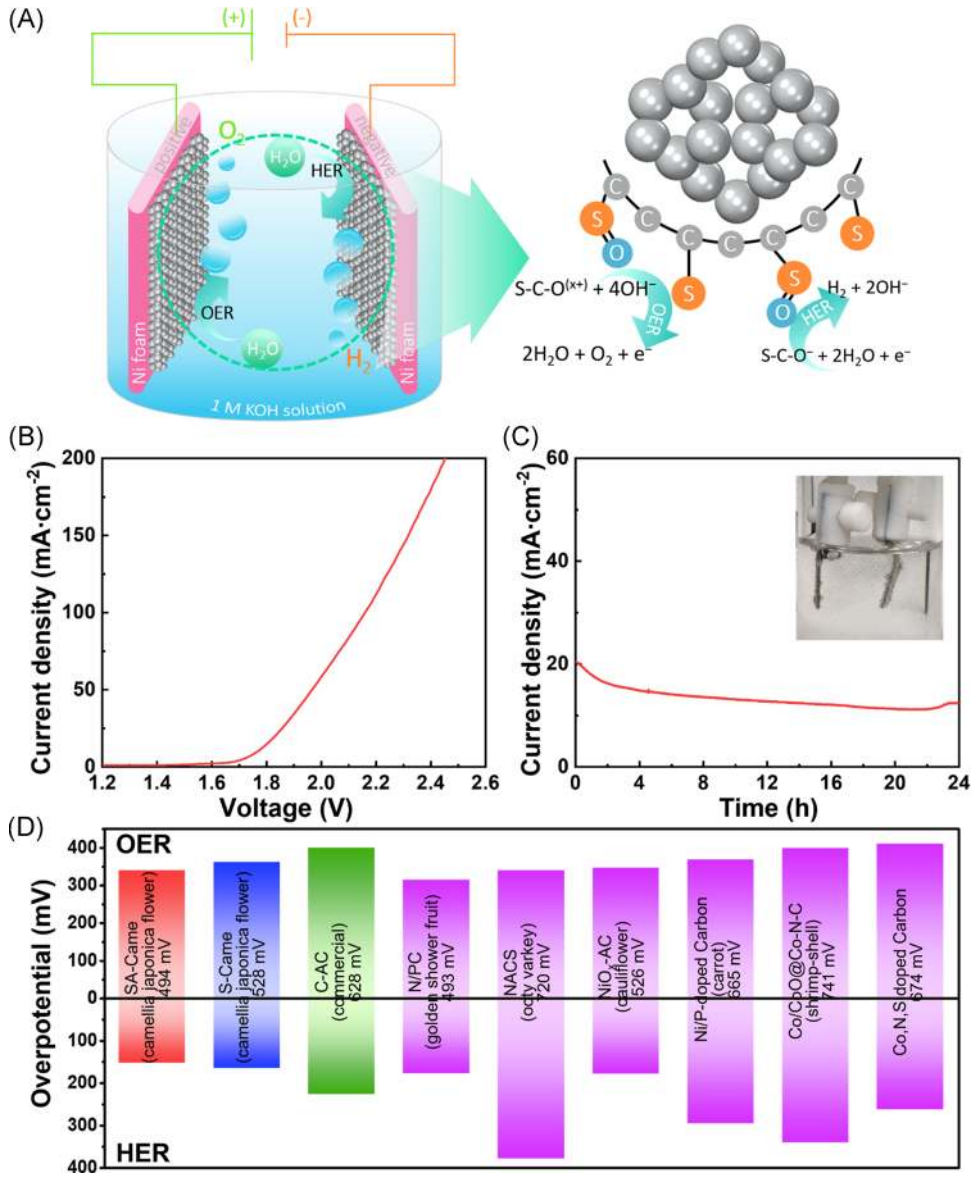


FIGURE 4 (A) Schematic representation of the S-AC water electrolyzer behavior. (B) LSV curve and (C) CA analysis of the fabricated S-AC water electrolyzer. The inset shows the electrolyzer with the visible evolution of oxygen and hydrogen bubbles. (D) OER and HER overpotential of sulfur-doped carbon, biomass-derived AC, and catalysts in this study. AC, activated carbon; CA, chronoamperometry; HER, hydrogen evolution reaction; LSV, linear sweep voltammetry; OER, oxygen evolution reaction

3.3 | Supercapacitor performance

Considering the satisfactory characterization and water-splitting performance of the SA-Came electrocatalyst, the performance of the as-synthesized samples for supercapacitor electrodes was also investigated. First, cyclic voltammetry (CV) analysis was conducted to differentiate the individual performances of the prepared SA-Came with respect to S-Came, C-AC, and bare Ni foam electrodes at a fixed scan rate of 10 mV s^{-1} in a negative potential range from 0 to −1.0 V versus Hg/HgO (Figure 5A). The AC electrodes showed a quasi-rectangular CV curve, which revealed a typical electrical double layer capacitance (EDLC), whereas the CV curves of the SA-Came sample showed some tiny humps, attributed to the pseudocapacitance arising from sulfur–carbon functional groups in the carbon framework. The partial redox activity shown by the SA-Came sample could be attributed to the partial charge-transfer contribution achieved by the presence of sulfur and oxygen functional groups in the adjacent carbon atoms. Further, the CV curves were measured to differentiate the individual performance of the SA-Came sample prepared under different experimental conditions (Figure S8). Comparatively, the SA-Came sample prominently covers a large current area that results in higher

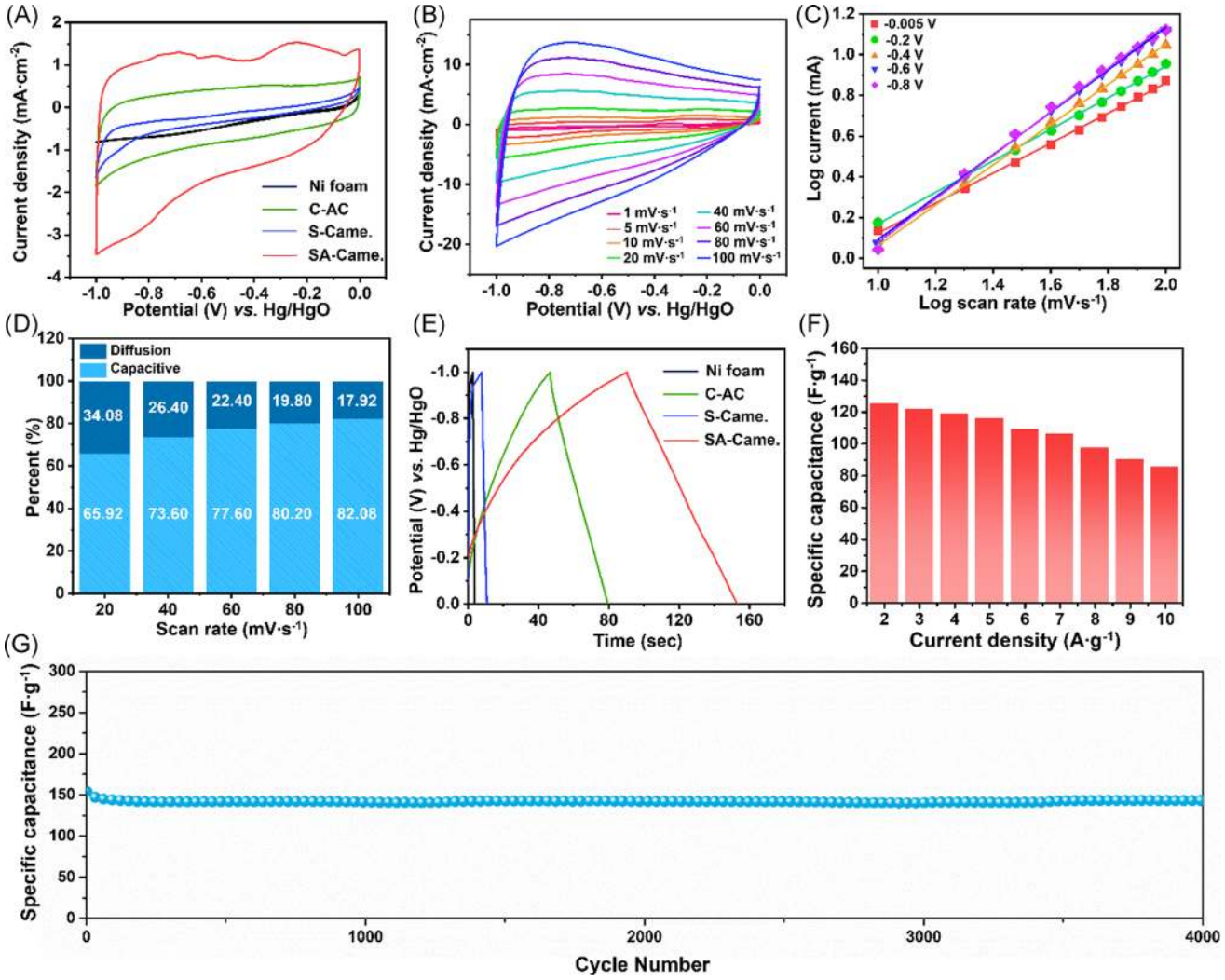


FIGURE 5 (A) CV curves at a scan rate of 10 mV s^{-1} of the bare Ni foam, C-AC, S-Came, and SA-Came in the potential range from –1 to 0 V versus Hg/HgO, (B) CV curves at various scan rates, (C) linear plot of log i versus log υ for SA-Came, (D) fractions of contributions at scan rates in the range of 20–100 mV s^{-1}, (E) GCD curves at a current density of 2 A g^{-1} of all prepared samples, (F) specific capacitance retention plot of GCD curves versus current density, and (G) cycling stability of SA-Came in the three-electrode system. C-AC, commercially available activated carbon; CV, cyclic voltammetry; GCD, galvanostatic charge/discharge; S-Came, sulfur-doped camellia; SA-Came, sulfur self-doped activated camellia

specific capacitance of 141.83 F g^{-1} than SA-Came(A9) (71.98 F g^{-1}) and SA-Came(A8) (104.96 F g^{-1}).

The energy storage properties of S-Came were evaluated by CV at various scan rates from a lower to a higher order (Figure 5B). The CV curves of SA-Came at low scan rates ranging from 1 to 10 mV s^{-1} are shown in Figure S9A. To further analyze the effect of capacitance control and diffusion control on the capacitance behavior, a more detailed quantitative analysis of the cyclic voltammetry curve was conducted. For SA-Came, a linear fitting analysis was performed on the logarithm of the scan rate and the logarithm of the current at different potentials (Figure 5C). Based on Equation S5, the calculated slope values at various potentials demonstrate that in the SA-Came electrode, capacitive-controlled EDLC behavior dominated. At a low scan rate, the observed anodic peak current values of SA-Came were plotted against their respective scan rates and root of scan rates (Figure S9B). The fitted anodic peak current values were linear with scan rates, also indicating that the capacitive behavior of SA-Came was a typical capacitive-controlled process. Furthermore, the contribution ratios of the capacitive and diffusion processes in the capacitance behavior were calculated based on Equation S6. Figure S9C shows that the capacitive mechanism was present mainly with a partial contribution from the diffusion mechanism at a scan rate of 100 mV s^{-1}. As shown in Figure 5D, the improved charge storage property

of the SA-Came electrode was because of the predominant contribution of the EDLC mechanism as well as the partial redox reaction. With an increase in the scan rate, the fraction of charges stored by the diffusion-controlled process decreased with the gradual increase in the capacitive contribution.

Then, galvanostatic charge/discharge (GCD) measurements were performed to investigate the charging and discharging behavior of the electrodes. Similar to the CV analysis, the GCD curves of the prepared SA-Came, S-Came, and C-AC, as well as bare nickel foam, were compared to differentiate the electrodes based on their performance (Figure 5E). The GCD curves revealed that the prepared SA-Came showed a higher specific capacitance (125.42 F g^{-1}) than S-Came (5.72 F g^{-1}), C-AC (65.75 F g^{-1}), and bare nickel foam (2.16 F g^{-1}) at a current density of 2 A g^{-1}. The GCD curves in Figure S10 show that SA-Came prepared under different experimental conditions shows a lower specific capacitance of 60.42 F g^{-1} (SA-Came(A9)) and 115.72 F g^{-1} (SA-Came(A8)) than that of SA-Came (125.42 F g^{-1}) at a current density of 2 A g^{-1}, respectively. Figure 5F shows the GCD curves of SA-Came at various current densities (2–10 A g^{-1}) to estimate its capacity retention behavior at higher current densities. The capacitance retention plot confirmed that SA-Came had enhanced capacitance retention: it retained 92.51% of its initial capacity at high current density compared to the auxiliary electrodes. In addition, SA-Came showed good cycling stability with a minimal loss in its initial capacity for approximately 4000 cycles at a current density of 5 A g^{-1} (Figure 5G).

To further evaluate SA-Came nanospheres for practical applications, a symmetrical hybrid supercapacitor was fabricated using an SA-Came electrode with a dual-electrode system (Figure 6A). The CV curves of the device were quasi-rectangular at various scan rates from 1 to 100 mV s^{-1} (Figures 6B and S11). The device stretched to a high cell voltage of 1.6 V, which is relatively higher than that reported for biomass-derived supercapacitor systems. The calculated specific capacity from the CV curve showed the highest specific capacity of 117.52 F g^{-1} at a scan rate of 1 mV s^{-1}. The GCD curves of the device obtained at various current densities from 1.0 to 4.0 A g^{-1} reached a cell voltage of 1.6 V with a quasi-triangular curve (Figure 6C).

Moreover, the specific capacity of the device calculated from the GCD curves was 77.7 F g^{-1} at a current density of 1.0 A g^{-1}. The energy and power densities of the device were calculated from the GCD curves. In this study, the highest energy density was 34.54 Wh kg^{-1} at a power density of 1600 W kg^{-1}. This result suggests that the SA-Came supercapacitor device showed a significantly improved energy density compared to other carbon-based composites ones. The Ragone plot of the SA-Came device confirmed its superiority over other reported artificial sulfur-doped, carbon-based, and biomass-derived supercapacitor devices (Figure 6D). Notably, the original sulfur-doped SA-Came electrode showed higher energy and power density values than the N and S-codoped catalysts. The detailed energy and power density values are listed in Table S1. Finally, the cycling stability of the device indicated high stability for approximately 15,000 cycles at a current density of 4.0 A g^{-1} with a significant capacity retention rate (98%) (Figure 6E). The device was utilized in real-time applications in white (3.5 V), yellow (2.1 V), blue (4.0 V), and green (2.2 V) light-emitting diode devices (inset images in Figure 6E).

The as-synthesized SA-Came electrocatalyst showed good electrochemical supercapacitor performance, which may be attributed to the high electrochemical surface area provided by the mesoporous structure and the fast charge-transfer process promoted by S-doping, thereby accelerating the redox reaction. For an in-depth understanding of the enhanced electrochemical performance of SA-Came, the effect of S-doping was investigated by density functional theory calculations: the adsorption energy, the population of electrons from the density of states (DOS), and plane-averaged charge density difference. By comparing the adsorption energies of adsorbing electrolyte ions (K^+) on the C-AC surface and the SA-Came surface, the effects of S-doping on the adsorption of K^+ were observed (Figure 7A). As the adsorption/desorption of K^+ ions from KOH aqueous electrolyte occurs during charging/discharging of a supercapacitor, we calculated the adsorption energies of K^+ ions on the active sites of C-AC and SA-Came. According to the classical Sabatier's principle, K^+ ions should bind neither too strongly nor weakly on the catalytic surface to avoid hindrance to the charge/discharge process. Thus, the adsorption energy of the K^+ ion should be nearly zero. As we mentioned in the study, SA-Came, consisting of S-containing reduced graphene oxide (rGO) and a-carbon, showed nearly zero adsorption energy on both active sites. Hence, it is obvious that charging/discharging will take place more efficiently on the surface of SA-Came than that on the surface of C-AC. The electrical conductivities of SA-Came and C-AC were compared by electron density of states (DOS). The electrical conductivity is related to the electron charge/discharge kinetics, meaning that the easier the movement of electrons, the better the electrocatalytic activities. Moreover, the DOS and plane-averaged charge density difference (Figure 7B) indicated that SA-Came has higher conductivity than C-AC. We can see that the number of electrons near the Fermi level of SA-Came is higher than that of C-AC, indicating that the electrons can move more easily in

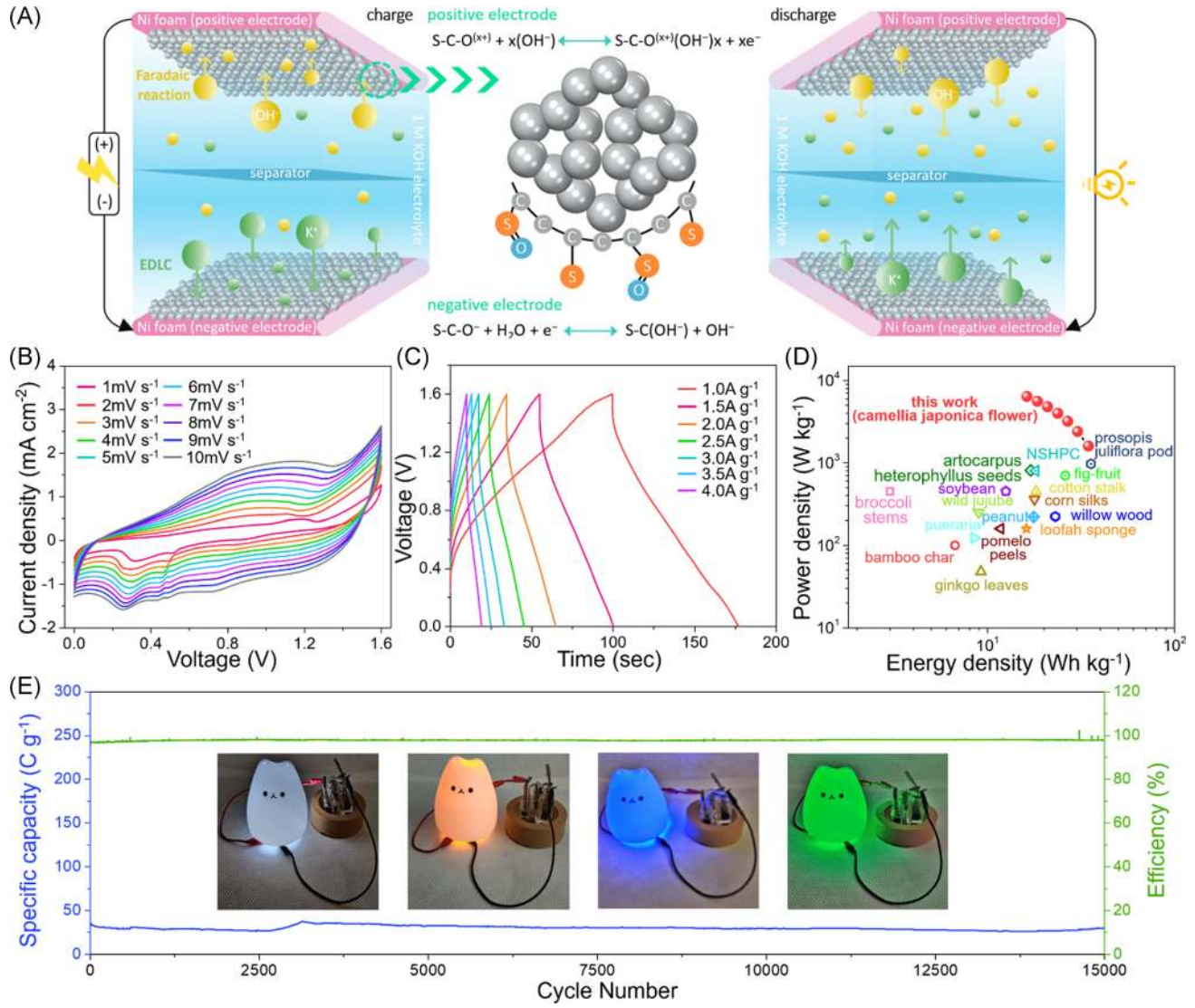


FIGURE 6 (A) Schematic charge mechanism of the SA-Came symmetric hybrid supercapacitor device. (B) CV curves of the fabricated supercapacitor at various scan rates. (C) GCD curves of the fabricated supercapacitor at various current densities. (D) Ragone plots of the fabricated supercapacitor. (E) Cycling stability and capacity efficiency of the fabricated supercapacitor. Inset: the fabricated supercapacitor being used in a real-time application. CV, cyclic voltammetry; GCD, galvanostatic charge/discharge; SA-Came, sulfur self-doped activated camellia

SA-Came. Thus, sulfur self-doping of SA-Came leads to stronger electrolyte adsorption and higher conductivity, which is preferred for boosting electrochemical performance.

Also, the built-in electric field can be formed by the difference of the work function between two different materials in a heterojunction structure. Especially, the large difference in the work function between S-consisting of rGO and a-carbon in SA-Came induced a larger magnitude of the built-in electric field in comparison to the case of C-AC. The formed built-in electric field of SA-Came can play two main roles in the performance of water splitting and a supercapacitor. It can behave as an attractive force to induce OH^- and H^+ on the catalyst surface of rGO and a-carbon, respectively, for enhancing water-splitting performance. Subsequently, OH^- ions, which are involved in the charging/discharging process, can be incorporated into the S-containing rGO/a-carbon heterostructure by the built-in electric field. They will result in a potential difference according to the OH^- ion concentration in the inner region of the heterojunction structure. It can promote the discharging process through the enhanced ability of OH^- desorption and consequently lead to improved supercapacitance. Therefore, we can conclude that the doped S atom of SA-Came significantly contributes to the enhanced multifunctional catalytic reactivity for water splitting and supercapacitors.

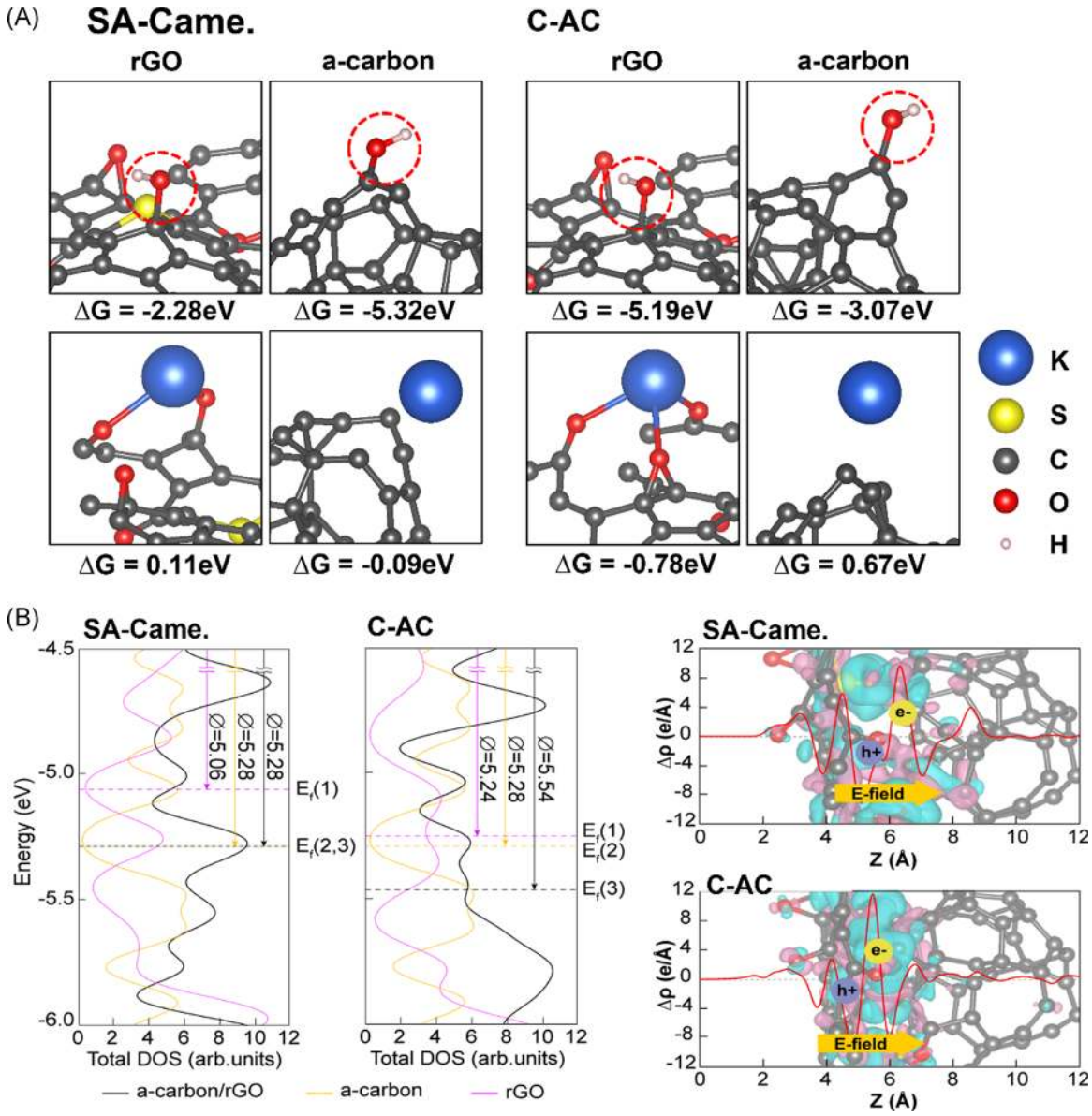


FIGURE 7 (A) Calculated K^+ and OH^- Gibbs free energies of SA-Came and C-AC. The blue, yellow, black, red, and pink balls represent K, S, C, O, and H atoms, respectively. (B) Calculated total density of states (TDOS) of S-AC and AC. The black lines represent the TDOS of the a-carbon/rGO heterostructure, which consists of rGO and a-carbon. The yellow and pink lines show the TDOS of a-carbon and rGO, respectively. Ø represents the work function. $E_f(1)$, $E_f(2)$, and $E_f(3)$ depict the Fermi energies of the heterostructure, a-carbon, and rGO with horizontal dotted lines, respectively. Plane-averaged charge density differences of S-AC and AC. The pink and blue regions denote the electron accumulation and depletion regions, respectively. The isovalue is set to 0.04 e/Bohr. The black, red, and yellow balls indicate C, O, and S atoms, respectively. AC, activated carbon; C-AC, commercially available activated carbon; rGO, reduced graphene oxide; SA-Came, sulfur self-doped activated camellia

4 | CONCLUSION

In summary, SA-Came was prepared using the solvothermal–pyrolysis method using camellia flower biomass as a raw material. In particular, with the self-doping of sulfur heteroatoms on the carbon skeleton, rapid charge transfer can be achieved in electrochemical reactions, which is favorable in supercapacitors and water-splitting applications. Compared with commercial activated carbon materials, SA-Came shows higher electrochemical activity. As a reliable electrode material, SA-Came showed high HER and OER performances with overpotentials of 154 and 362 mV to reach a current density of 10 mA cm^{-2} and a low Tafel slope (89.92 mV dec^{-1}). When assembled as a dual-electrode water-splitting system, the device was driven with a voltage of 1.76 V at 10 mA cm^{-2}. Additionally, it showed a specific capacitance of

125.42 $F g^{-1}$ at a current density of 2 $A g^{-1}$. The obtained sulfur self-doped biochar derived from camellia flowers not only has good potential for energy conversion and storage devices but also provides valuable insights into the efficient utilization of waste biomass.

ACKNOWLEDGMENTS

The authors are grateful for the financial support from the National Research Foundation of Korea funded by the Ministry of Science and the Republic of Korea (2020R1A2C2006077, 2021R1A5A1030054, 2021R1A4A1024129, and 2022R1A2C1012419) and the Creative Materials Discovery Program through the National Research Foundation of Korea (NRF-2016M3D1A1021141). This work was also supported by the Technology Innovation Program (Development of Superalloy Powder and Parts Manufacturing Technology for Additive Manufacturing) (20213030040590) funded by the Ministry of Trade, Industry & Energy (MOTIE, Korea).

CONFLICT OF INTEREST

The authors declare no conflict of interest.

ORCID

Subramani Surendran https://orcid.org/0000-0003-0750-3199
Chang Hyuck Choi https://orcid.org/0000-0002-2231-6116
Uk Sim https://orcid.org/0000-0001-7767-495X

REFERENCES

1. Pang J, Mendes RG, Bachmatiuk A, et al. Applications of 2D MXenes in energy conversion and storage systems. *Chem Soc Rev*. 2019;48(1):72-133.
2. Abdolahi B, Gholivand MB, Shamsipur M, Amiri M. Engineering of nickel-cobalt oxide nanostructures based on biomass material for high performance supercapacitor and catalytic water splitting. *Int J Energy Res*. 2021;45(9):12879-12897.
3. You B, Sun Y. Innovative strategies for electrocatalytic water splitting. *Acc Chem Res*. 2018;51(7):1571-1580.
4. Roger I, Shipman MA, Symes MD. Earth-abundant catalysts for electrochemical and photoelectrochemical water splitting. *Nat Rev Chem*. 2017;1(1):0003.
5. Li C, Luo Z, Wang T, Gong J. Surface, bulk, and interface: rational design of hematite architecture toward efficient photoelectrochemical water splitting. *Adv Mater*. 2018;30(30):1707502.
6. Li X-P, Zheng L-R, Liu S-J, et al. Heterostructures of NiFe LDH hierarchically assembled on MoS_2 nanosheets as high-efficiency electrocatalysts for overall water splitting. *Chin Chem Lett*. In press; doi:10.1016/j.cclet.2021.12.095
7. Chen J, Long Q, Xiao K, et al. Vertically-interlaced NiFeP/MXene electrocatalyst with tunable electronic structure for high-efficiency oxygen evolution reaction. *Sci Bull*. 2021;66(11):1063-1072.
8. Zhang B, Zheng Y, Ma T, et al. Designing MOF nanoarchitectures for electrochemical water splitting. *Adv Mater*. 2021;33(17):2006042.
9. Feng J, Lv F, Zhang W, et al. Iridium-based multimetallic porous hollow nanocrystals for efficient overall-water-splitting catalysis. *Adv Mater*. 2017;29(47):1703798.
10. Wu Z, Zhao Y, Wu H, et al. Corrosion engineering on iron foam toward efficiently electrocatalytic overall water splitting powered by sustainable energy. *Adv Funct Mater*. 2021;31(17):2010437.
11. Xiong C, Li B, Lin X, et al. The recent progress on three-dimensional porous graphene-based hybrid structure for supercapacitor. *Compos B Eng*. 2019;165:10-46.
12. Liu H, Liu X, Wang S, Liu HK, Li L. Transition metal based battery-type electrodes in hybrid supercapacitors: a review. *Energy Storage Mater*. 2020;28:122-145.
13. Li Q, Zheng S, Xu Y, Xue H, Pang H. Ruthenium based materials as electrode materials for supercapacitors. *Chem Eng J*. 2018;333:505-518.
14. Xiao K, Zhao S-L, Cao M, Zhang L, Li N, Liu ZQ. Electron affinity regulation on ultrathin manganese oxide nanosheets toward ultra-stable pseudocapacitance. *J Mater Chem A*. 2020;8(44):23257-23264.
15. Xiao K, Xiao T-Q, Zhang Y, et al. In situ evolution of the active phase on stainless steel mesh toward a cost-effective bifunctional electrode for energy storage and conversion. *Chem Commun*. 2019;55(17):2513-2516.
16. Sharma V, Narayan Pan U, Ibomcha Singh T, Kumar Das A, Hoon Kim N, Hee Lee J. Pragmatically designed tetragonal copper ferrite super-architectures as advanced multifunctional electrodes for solid-state supercapacitors and overall water splitting. *Chem Eng J*. 2021;415:127779.
17. Penke YK, Sinha P, Yadav AK, Ramkumar J, Kar KK. Al^{3+}-doped 3d-transitional metal (Mn/Cu) ferrite impregnated rGO for PEC water-splitting/supercapacitor electrode with oxygen vacancies and surface intercalation aspects. *Compos B Eng*. 2020;202:108431.
18. Ye J, Li Q, Ma X, et al. $CoNi_2S_4$ nanoparticle on carbon cloth with high mass loading as multifunctional electrode for hybrid supercapacitor and overall water splitting. *Appl Surf Sci*. 2021;554:149598.
19. Jiang Y, Li J, Jiang Z, et al. Large-surface-area activated carbon with high density by electrostatic densification for supercapacitor electrodes. *Carbon*. 2021;175:281-288.
20. Kandasamy M, Sahoo S, Nayak SK, Chakraborty B, Rout CS. Recent advances in engineered metal oxide nanostructures for supercapacitor applications: experimental and theoretical aspects. *J Mater Chem A*. 2021;9(33):17643-17700.
21. Yang HJ, Lee J-W, Seo SH, et al. Fully stretchable self-charging power unit with micro-supercapacitor and triboelectric nanogenerator based on oxidized single-walled carbon nanotube/polymer electrodes. *Nano Energy*. 2021;86:106083.
22. Gu X, Chen Z, Li Y, et al. Polyaniline/carbon dots composite as a highly efficient metal-free dual-functional photoassisted electrocatalyst for overall water splitting. *ACS Appl Mater Interfaces*. 2021;13(21):24814-24823.

23. Zhang LL, Zhao XS. Carbon-based materials as supercapacitor electrodes. *Chem Soc Rev*. 2009;38(9):2520-2531.
24. Liu W-J, Jiang H, Yu H-Q. Emerging applications of biochar-based materials for energy storage and conversion. *Energy Environ Sci*. 2019;12(6):1751-1779.
25. Woolf D, Amonette JE, Street-Perrott FA, Lehmann J, Joseph S. Sustainable biochar to mitigate global climate change. *Nat Commun*. 2010;1:56.
26. Altinci OC, Demir M. Beyond conventional activating methods, a green approach for the synthesis of biocarbon and its supercapacitor electrode performance. *Energy Fuels*. 2020;34(6):7658-7665.
27. Humagain G, MacDougal K, MacInnis J, et al. Highly efficient, biochar-derived molybdenum carbide hydrogen evolution electrocatalyst. *Adv Energy Mater*. 2018;29(8):1801461.
28. Long S, Feng Y, He F, et al. Biomass-derived, multifunctional and wave-layered carbon aerogels toward wearable pressure sensors, supercapacitors and triboelectric nanogenerators. *Nano Energy*. 2021;85:105973.
29. Zhou H, Deng Z, Liu T, et al. In situ controlled synthesis of porous Fe–N–C materials from oily sludge by chlorinating calcination and their novel application in supercapacitors. *Environ Sci Nano*. 2020;7(12):3814-3823.
30. Wan Z, Sun Y, Tsang DCW, et al. Customised fabrication of nitrogen-doped biochar for environmental and energy applications. *Chem Eng J*. 2020;401:126136.
31. Cao X, Li Z, Chen H, et al. Synthesis of biomass porous carbon materials from bean sprouts for hydrogen evolution reaction electrocatalysis and supercapacitor electrode. *Int J Hydrog Energy*. 2021;46(36):18887-18897.
32. Yang J, Liu K-X, Liu Q-Y, Zheng XC. Biomass waste-derived mesopore-dominant porous carbon for high-efficiency capacitive energy storage. *J Alloys Compd*. 2021;885:161218.
33. Zhong K, Li M, Yang Y, et al. Nitrogen-doped biochar derived from watermelon rind as oxygen reduction catalyst in air cathode microbial fuel cells. *Appl Energy*. 2019;242:516-525.
34. Oh W-D, Lisak G, Webster RD, et al. Insights into the thermolytic transformation of lignocellulosic biomass waste to redox-active carbocatalyst: durability of surface active sites. *Appl Catal B*. 2018;233:120-129.
35. Cao L, Li H, Xu Z, et al. Camellia pollen-derived carbon with controllable N content for high-performance supercapacitors by ammonium chloride activation and dual N-doping. *ChemNanoMat*. 2021;7(1):34-43.
36. Escobar B, Martínez-Casillas DC, Pérez-Salcedo KY, et al. Research progress on biomass-derived carbon electrode materials for electrochemical energy storage and conversion technologies. *Int J Hydrog Energy*. 2021;46(51):26053-26073.
37. Tabak A, Sevimli K, Kaya M, Çağlar B. Preparation and characterization of a novel activated carbon component via chemical activation of tea woody stem. *J Therm Anal Calorim*. 2019;138:3885-3895.
38. Rahmawati F, Ridassepri AF, Wijayanta AT, et al. Carbon from bagasse activated with water vapor and its adsorption performance for methylene blue. *Appl Sci*. 2021;11(2):678.
39. Köseoğlu E, Akmil-Başar C. Preparation, structural evaluation and adsorptive properties of activated carbon from agricultural waste biomass. *Adv Powder Technol*. 2015;26(3):811-818.
40. Rehman A, Nazir G, Yop Rhee K, Park SJ. A rational design of cellulose-based heteroatom-doped porous carbons: promising contenders for CO_2 adsorption and separation. *Chem Eng J*. 2021;420:130421.
41. Mao H, Tang J, Chen J, et al. Designing hierarchical nanoporous membranes for highly efficient gas adsorption and storage. *Sci Adv*. 2020;6(41):eabb0694.
42. Wang Y, Zhang M, Shen X, et al. Biomass-derived carbon materials: controllable preparation and versatile applications. *Small*. 2021;17(40):2008079.
43. Zhang Y, Deng L, Hu H, et al. Pomelo peel-derived, N-doped biochar microspheres as an efficient and durable metal-free ORR catalyst in microbial fuel cells. *Sustainable Energy Fuels*. 2020;4(44):1642-1653.
44. Khan TA, Saud AS, Jamari SS, Rahim MHA, Park JW, Kim HJ. Hydrothermal carbonization of lignocellulosic biomass for carbon rich material preparation: a review. *Biomass Bioenergy*. 2019;130:105384.
45. Kim B, Choi O, Shim K. Chemical composition characteristics according to the collection period of camellia leaves. *Korean J Food Nutr*. 2005;34(5):681-686.
46. Pereira AG, Garcia-Perez P, Cassani L, et al. Camellia japonica: a phytochemical perspective and current applications facing its industrial exploitation. *Food Chem: X*. 2022;13:100258.
47. Qiu T, Yang J-G, Bai X-J, Wang YL. The preparation of synthetic graphite materials with hierarchical pores from lignite by one-step impregnation and their characterization as dye absorbents. *RSC Adv*. 2019;9(22):12737-12746.
48. Ferrari AC, Robertson J. Interpretation of Raman spectra of disordered and amorphous carbon. *Phys Rev B*. 2000;61(20):14095-14107.
49. Borghei M, Laocharoen N, Kibena-Põldsepp E, et al. Porous N,P-doped carbon from coconut shells with high electrocatalytic activity for oxygen reduction: alternative to Pt-C for alkaline fuel cells. *Appl Catal B*. 2017;204:394-402.
50. Lin G, Ma R, Zhou Y, Liu Q, Dong X, Wang J. KOH activation of biomass-derived nitrogen-doped carbons for supercapacitor and electrocatalytic oxygen reduction. *Electrochim Acta*. 2018;261:49-57.
51. Khalid M, Varela H. A general potentiodynamic approach for red phosphorus and sulfur nanodot incorporation on reduced graphene oxide sheets: metal-free and binder-free electrodes for supercapacitor and hydrogen evolution activities. *J Mater Chem A*. 2018;6(7):3141-3150.
52. Liu Y, Xiao Z, Liu Y, Fan LZ. Biowaste-derived 3D honeycomb-like porous carbon with binary-heteroatom doping for high-performance flexible solid-state supercapacitors. *J Mater Chem A*. 2018;6(1):160-166.
53. Zou X, Huang X, Goswami A, et al. Cobalt-embedded nitrogen-rich carbon nanotubes efficiently catalyze hydrogen evolution reaction at all pH values. *Angew Chem Int Ed*. 2014;53(17):4372-4376.
54. Si W, Zhou J, Zhang S, Li S, Xing W, Zhuo S. Tunable N-doped or dual N, S-doped activated hydrothermal carbons derived from human hair and glucose for supercapacitor applications. *Electrochim Acta*. 2013;107:397-405.

55. Zou B-X, Gao Y, Liu B, Yu Y, Lu Y. Three dimensional heteroatom-doped carbon composite film for flexible solid-state supercapacitors. *RSC Adv*. 2016;6(6):4483-4489.
56. Lin T, Chen IW, Liu F, et al. Nitrogen-doped mesoporous carbon of extraordinary capacitance for electrochemical energy storage. *Science*. 2015;350(6267):1508-1513.
57. Li J, Zhang G, Fu C, Deng L, Sun R, Wong CP. Facile preparation of nitrogen/sulfur co-doped and hierarchical porous graphene hydrogel for high-performance electrochemical capacitor. *J Power Sources*. 2017;345:146-155.
58. Sun L, Zhou H, Li L, et al. Double soft-template synthesis of nitrogen/sulfur-codoped hierarchically porous carbon materials derived from protic ionic liquid for supercapacitor. *ACS Appl Mater Interfaces*. 2017;9(31):26088-26095.
59. Kim JK, Park MJ, Kim SJ, et al. Balancing light absorptivity and carrier conductivity of graphene quantum dots for high-efficiency bulk heterojunction solar cells. *ACS Nano*. 2013;7(8):7207-7212.
60. Sathiskumar C, Ramakrishnan S, Vinothkannan M, Rhan Kim A, Karthikeyan S, Yoo DJ. Nitrogen-doped porous carbon derived from biomass used as trifunctional electrocatalyst toward oxygen reduction, oxygen evolution and hydrogen evolution reactions. *Nanomaterials*. 2020;10(1):76.
61. Prabu N, Kesavan T, Maduraiveeran G, Sasidharan M. Bio-derived nanoporous activated carbon sheets as electrocatalyst for enhanced electrochemical water splitting. *Int J Hydrog Energy*. 2019;44(36):19995-20006.
62. Hoang VC, Gomes VG, Dinh KN. Ni- and P-doped carbon from waste biomass: a sustainable multifunctional electrode for oxygen reduction, oxygen evolution and hydrogen evolution reactions. *Electrochim Acta*. 2019;314:49-60.
63. Hoang VC, Dinh KN, Gomes VG. Hybrid Ni/NiO composite with N-doped activated carbon from waste cauliflower leaves: a sustainable bifunctional electrocatalyst for efficient water splitting. *Carbon*. 2020;157:515-524.
64. Zhang X, Liu R, Zang Y, et al. Co/CoO nanoparticles immobilized on Co–N-doped carbon as trifunctional electrocatalysts for oxygen reduction, oxygen evolution and hydrogen evolution reactions. *Chem Commun*. 2016;52(35):5946-5949.
65. Chen J, Qiu L, Li Z, et al. Chitin-derived porous carbon loaded with Co, N and S with enhanced performance towards electrocatalytic oxygen reduction, oxygen evolution, and hydrogen evolution reactions. *Electrochim Acta*. 2019;304:350-359.

SUPPORTING INFORMATION

Additional supporting information can be found online in the Supporting Information section at the end of this article.

How to cite this article: Xia C, Surendran S, Ji S, et al. A sulfur self-doped multifunctional biochar catalyst for overall water splitting and a supercapacitor from Camellia japonica flowers. *Carbon Energy*. 2022;4:491-505.
doi:10.1002/cey2.207